

# Creep and tensile behaviors of Fe–Cr–Al foils and laser microwelds at high temperature

Haitham El Kadiri<sup>a,\*</sup>, Yves Bienvenu<sup>b</sup>, Kiran Solanki<sup>a</sup>,  
Mark F. Horstemeyer<sup>a</sup>, Paul T. Wang<sup>a</sup>

<sup>a</sup> Center for Advanced Vehicular Systems, Mississippi State University, MS 39762-9627, USA

<sup>b</sup> Ecole des Mines de Paris, Centre des Matériaux, CNRS UMR 7633, BP 87, 91003 Evry, France

Received 20 April 2005; received in revised form 1 November 2005; accepted 21 November 2005

## Abstract

We examine a Fe–Cr–Al foil-based material and a continuous-wave laser weld generated in ultra-fine “keyhole” mode undergoing tensile and creep-tension tests over a temperature range of 25–1000 °C. At all temperatures, the bead exhibits superior tensile resistance than the base material due to a homogenous reprecipitation of fine aluminum nitrides, AlN, but creeps faster at 900 °C, because of a finer-grained microstructure scarcely undergoing secondary recrystallization. Under tensile loading, the base material ductility is higher than that of the weld and increases with increasing temperature, but drops above 900 °C due to faster grain growth and chromium carbide precipitation. The base material stress–strain curves exhibit concomitant decrease of the yield point effect magnitude and increase of the strain hardening rate with the temperature, but only up to a critical value, which decreases with increasing the strain rate. After vanishing at this critical temperature, the yield point effect reappears upon the onset of sample necking responsible for the ensuing continuous decrease of the engineering stress. The strain–stress curves of laser welds show no yield point effect and the work hardening persists at all temperatures. Under creep-tension, the weld shows a strong anisotropic behavior, and the highest flow rate is recorded for welds oriented parallel to the loading direction, because of a more important cavity nucleation.

© 2006 Elsevier B.V. All rights reserved.

**Keywords:** Catalytic converter; Fe–Cr–Al foil; Laser welding; Finite element simulations; High temperature; Creep; Tensile; SEM; TEM

## 1. Introduction

Although Fe–Cr–Al-foil substrates are associated with a less cost-effective catalytic converter monolith design than extruded ceramics, they offer decisive technical advantages: less thermal inertia, shorter light off time, less risk of overheating, lower back-pressure, superior performance at elevated temperatures, easier recycling and possibility to manufacture large size components for heavy duty applications [1]. These properties allow the metallic converter to be electrically preheated and positioned closer to the engine, thereby increasing the conversion rate for closer compliance with the Zero Emission Vehicle (ZEV) standards becoming effective in 2005 [2]. However, these measures lead to a more severe thermal loading of the material and structure at the risk of not producing high quality and affordable systems required by the fast-growing market and global competition [3]. These engineering challenges drive the need for

advanced design control at two key-manufacturing phases:

- The shaping process of the monolith base material, a ferritic refractory stainless steel, usually Fe–Cr–Al with 20 wt.% Cr and 5 wt.% Al with a foil thickness coming down from 200 to 25 μm;
- The joining process used to make the spiraled monolith into a “rigid” structure using for metallurgical fixture for a casing tube, also a refractory stainless steel. These aspects will be treated in a different paper.

In addition to a shorter total Al depletion, reducing the foil thickness results in a more pronounced creep-buckling of the foil under the compressive growth stresses associated with the inward growth mechanism of the oxide, which predominates in the range of very high temperature ( $\geq 1100$  °C). The foil buckling, on one hand, decreases the conversion efficiency of the catalyst by sagging the honeycomb cells, and on the other hand promotes scale spallation that results in a faster onset of the breakaway oxidation. Even in the range of low temperature

\* Corresponding author. Tel.: +1 662 325 5568; fax: +1 662 325 5433.  
E-mail address: elkadiri@cava.msstate.edu (H. El Kadiri).

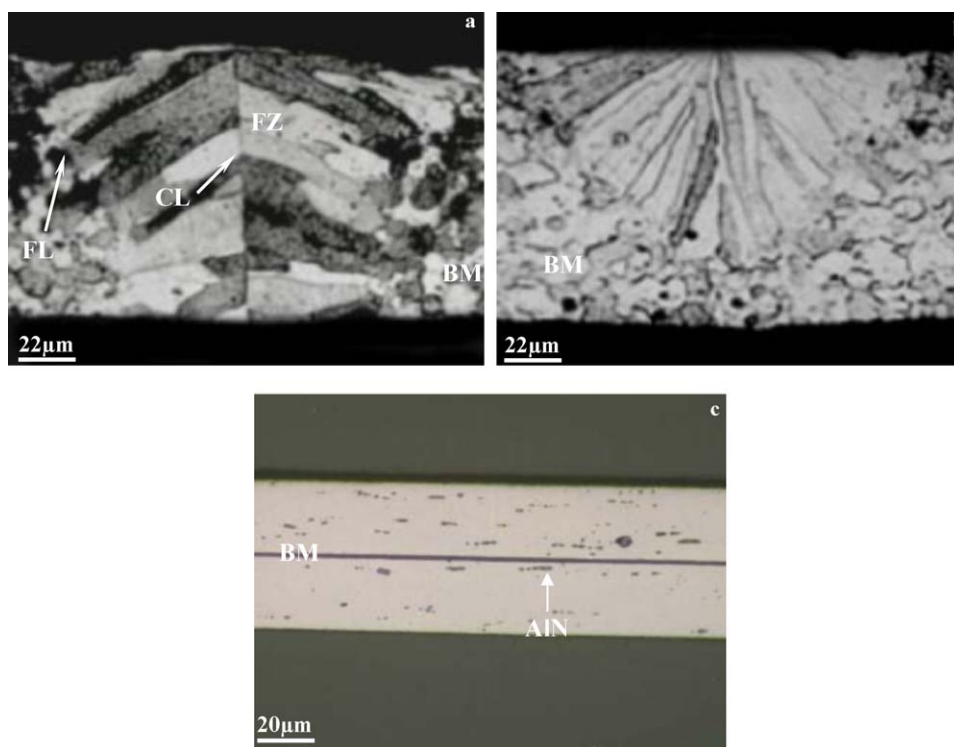


Fig. 1. Optical micrographs of etched cross-section microstructures laser beads and BM: (a) full penetration with  $P = 400$  W and  $V = 37$  m/min, (b) partial penetration with  $P = 400$  W and  $V = 46$  m/min, and (c) polished cross-section of two foils down to  $1/4 \mu\text{m}$ , displaying alignment trains of AlN.

(<1100 °C), where the substrate undergoes much lower creep, the systematic tensile growth stresses induce dramatic interfacial cavities that grow independently of the substrate Al-reservoir. A reduction of the foil thickness will consequently lead to more severe damage progression and earlier failure of the component. Besides these effects on the behavior and fracture toughness of the foil, growth stresses in the foil directly affect the oxidation kinetics, and the diffusion fluxes are driven by both composition and heterogeneous stress gradients. Moreover, the relaxation rate of growth stresses by creep influences the oxidation kinetics since creep facilitates the phase transformation rates of the fast-growing metastable aluminas by promoting interface recession [4]. Fundamental understanding of the mechanical properties of Fe–Cr–Al foils is therefore critical for developing new affordable alumina-forming iron-based alloys, allowing thinner foils to be manufactured and used with adequate formability and lifetime expectations [5–7]. The main scope of this paper is to study the mechanical properties of the Fe–Cr–Al foil and a laser beam weld in an effort to validate an autogenous laser beam welding for assembling the honeycomb-style catalyst during the coiling of the monolith in the “flying optics” principle [8–11]. We examine and compare the mechanical properties of the base material (BM) and an optimized laser beam condition-generated microstructure through tensile tests over a temperature range of 25–1000 °C and creep-tension tests at 900 °C over a stress range of 1–40 MPa. The results are elucidated from microscopical observations and analyses using optical microscope (OM), scanning electron microscope (SEM), transmission electron microscope (TEM), and electron probe microanalysis (EPMA) techniques.

## 2. Laser welding experiments

A 400 W FEHA SM 400P CO<sub>2</sub> gas transport laser delivering a very narrow beam with a maximum diameter of 70 μm for a 30 mm focal length was used to weld two foils of 45 μm without noticeable morphological defects. Bead-on-plate welding tests were performed on a 95 μm thick Fe–Cr–Al foil. This laser offers a moving lens up to 100 m/min and delivers a beam with Gaussian-distribution energy.

The best welding condition corresponds to a peak power of 400 W and a welding speed of 37 m/min. This condition generates a fusion zone (FZ) 100 μm large at the upper face and 70 μm wide at the bottom side (Fig. 1a and b). All the weld lines were achieved at the focal point and a 10 l/min argon shielding gas was used to limit oxidation, with a nozzle located at the rear part of the melting pool. A four-point clamping tool with a 2 mm-large full-penetrated window was used to minimize the focal distance variation along the welding track. Prior to welding, the samples were ultrasonically cleaned in acetone and dried.

## 3. Base material and laser weld microstructures

### 3.1. Crude microstructures

#### 3.1.1. Base material

The Fe–Cr–Al alloy is a Sandvik 0C404 type with a low interstitial (C + N) level, “co-doped” with mishmetal (Ce + La), cold rolled down to 45 and 95 μm and annealed. Quantitative analysis of major and trace elements with Energy and Wavelength Dispersive X-ray analyses (EDS and WDS, respectively)

Table 1  
Chemical composition in wt.%

	Fe	Cr	Al	C+N	Si	Mn/Mg	Ti	P	S	Ce	La
Sandvik's data	Bal.	20.3	5.5	0.016	0.22	0.28/0.2		0.014	<0.0005	0.043	
EPMA results	73.3	20.5	5.18		0.19	0.27/0.2	0.007	0.015	0.0028	0.310	0.015

and EPMA performed on cross-sectional specimens polished down to  $1/4 \mu\text{m}$  are presented in Table 1 in comparison with the chemical composition data provided by the steel-producer. The trace element contents are averaged over 10 analyzed-windows of  $50 \mu\text{m} \times 50 \mu\text{m}$  surface area. These analyses reveal the presence of the main minor elements: Si, Ti, Mn, Mg, Si, Ce and La. Silicon reinforces the stability of the  $\alpha$ -ferrite phase and increases the creep resistance. Titanium is an efficient stabilizer of carbon, but can also assist aluminum to precipitate nitrogen in order to avoid excessive growth of the AlN particles detrimental

for the foil formability during the rolling process. Mg and Mn modify the chemical activity of carbon, while Ce and La, in form of mishmetal, promote the adherence of the oxide layer and can have a beneficial effect on the oxidation kinetics as well.

Annealed Fe–Cr–Al foil shows a fine equiaxed-grains microstructure (Fig. 1b) with enhanced precipitation of AlN and mishmetal-rich particles preferentially aligned with the rolling direction (Fig. 1c). The distribution and size of AlN particles are very irregular although the studied foil samples were extracted from the same drum. Chromium carbides and

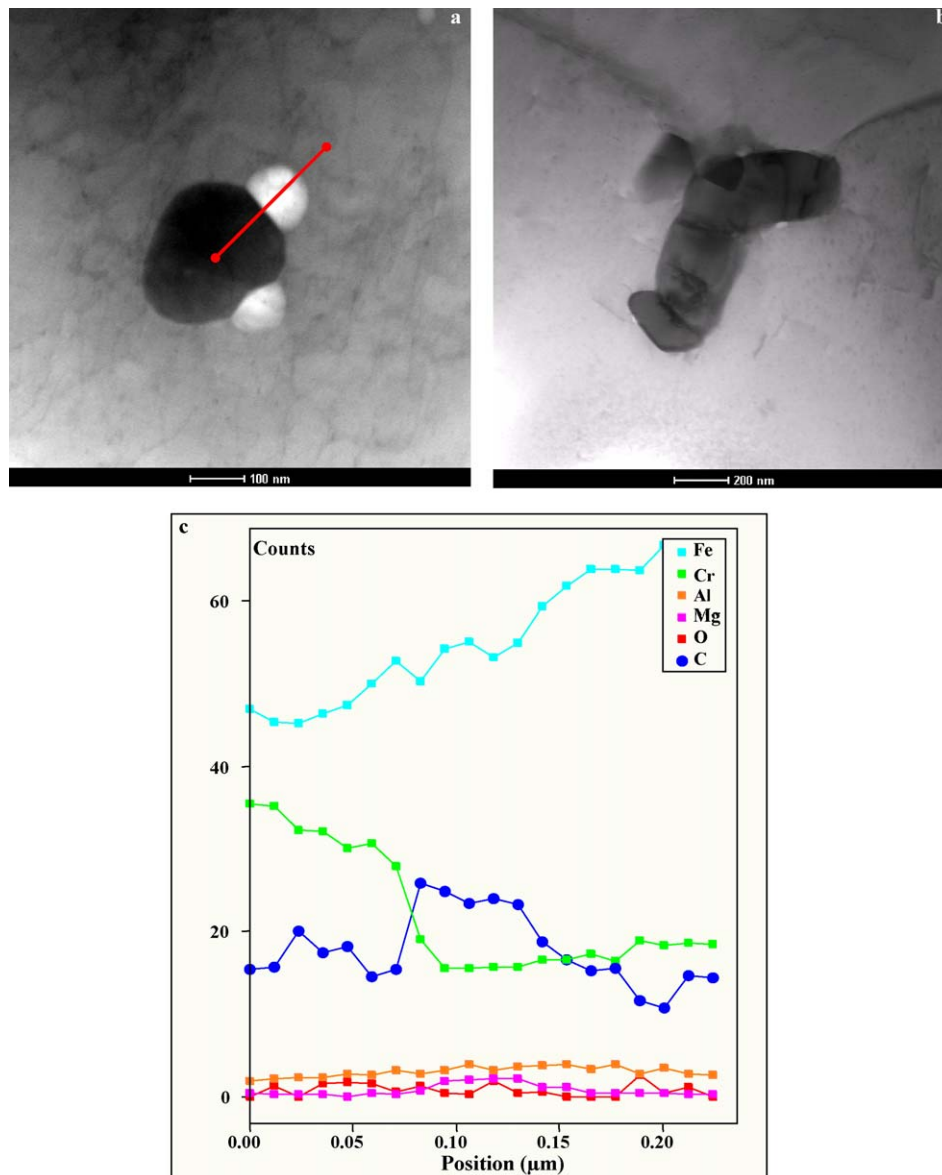


Fig. 2. (a) TEM dark-field image of the BM revealing heterogeneous nucleation on MgC on  $\text{Cr}_{23}\text{C}_6$ , (b) TEM dark-field image of the BM revealing intergranular  $\text{Cr}_{23}\text{C}_6$ , and (c) TEM chemical analyses along the line depicted in Fig. 5a, the beam diameter was 5 nm.

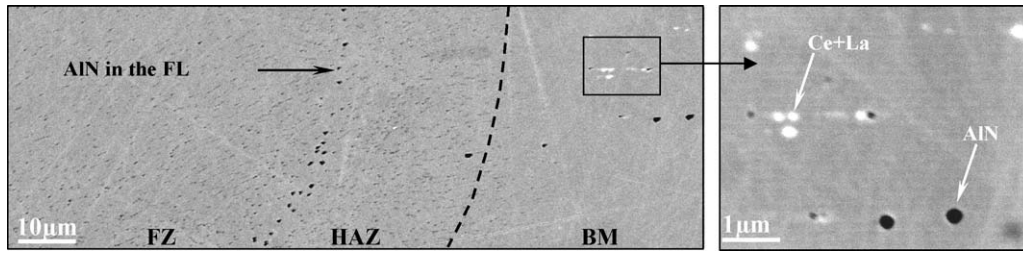


Fig. 3. SEM views of cross-sectional samples in backscattered electron mode: (a) AIN precipitation in the FZ and heat affected zone (HAZ) and (b) AIN and mishmetal-rich precipitates in the BM aligned with rolling direction.

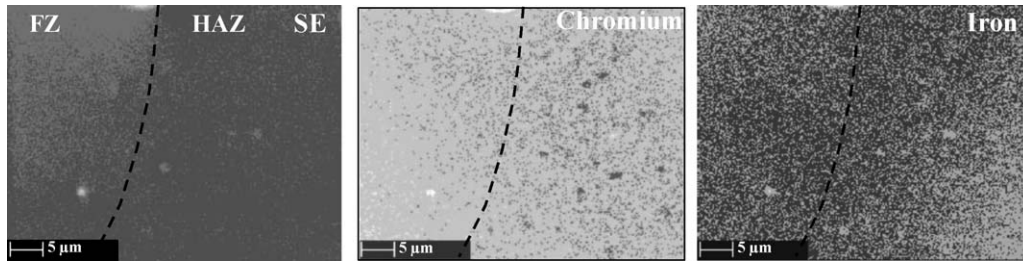


Fig. 4. EPMA X-ray maps of FZ and HAZ bulk cross-sections showing enhanced precipitation of chromium-rich particles (mainly chromium carbides).

Mg–Fe–Cr enriched carbide particles are also present in the matrix in the form of very small globules (200 nm maximum size) that can be only detected by TEM micrographs and analyses (Fig. 2).

### 3.1.2. Laser welds

Fig. 1a and b shows that the weld solidification is fine-grained in the vicinity of the fusion line (FL), but mostly dendritic toward the center line (CL). The high peak temperatures and fast cooling rates experienced by the FZ seem to have led to the total dissolution of the initial stabilizer-secondary phases, causing the carbon and nitrogen to return in solid solution [9,10]. The dissolution of nitrogen is evidenced by the fine and homogeneous AIN “re-precipitation” (<300 nm) in the FZ matrix (Fig. 3a and b), while that of carbon can be supported by the fact that chromium rich-particle formation only occurs in the HAZ (Fig. 4). Indeed, carbon which is more available for precipitation in the HAZ than in the BM must be more available in the FZ than in the HAZ, since the latter experienced lower temperatures than that in the FZ.

Quantitative profile analyses of trace elements using EPMA techniques reveal a substantial Ce and La enrichment near the external surfaces of the FZ (Fig. 5). This may result from the transport of enriched melt by the Marangoni-induced down and upper flows and amplified by the hydrodynamic flow pulsations associated with the keyhole mode [10]. The chemical state of Ce + La in the FZ has not been formally identified, but it may correspond to a solid solution state.

### 3.2. Base material and laser weld microstructures at high temperatures

We performed heat treatment tests at approximately 900 and 1100 °C with various soaking periods in order to study the grain growth phenomena that take place in the FZ in comparison with those occurring in the BM. In order to reduce the effect

of the thermally grown oxide layer on the grain growth kinetics, all the annealing tests were carried out in secondary vacuum ( $\approx 10^{-6}$  Pa). This study is important to understand the difference in creep behavior between the two materials, and also to elucidate the difference in oxidation kinetics that may depend on the substrate grain size especially in the temperature range where the scaling rate is controlled by a cationic diffusion phenomenon [11].

Figs. 6 and 7 depict typical microstructures obtained after ageing in vacuum. The main point to be taken from these microstructures is the insensitivity of the FZ to secondary recrystallization although the matrix is ferritic. This intriguing behavior can be explained either by (i) the elongated profiles of the grains whose curvatures are not high enough to stimulate visible migration of grain boundaries or/and by (ii) enhanced pinning of the grain boundaries by the AIN precipitates homogeneously speckled in the matrix. The first of these two suggested mechanisms is elucidated by Fig. 6b. In fact, at 1100 °C the grain

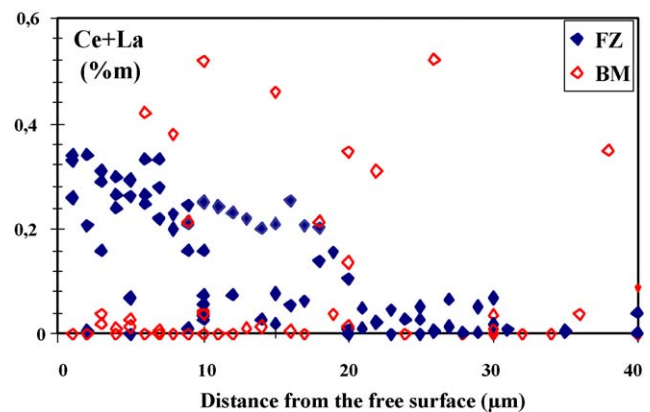


Fig. 5. Ce+La content in the BM and FZ measured by EPMA in the trace of element mode, observe substantial Ce and La enrichment near the external surfaces of the FZ.

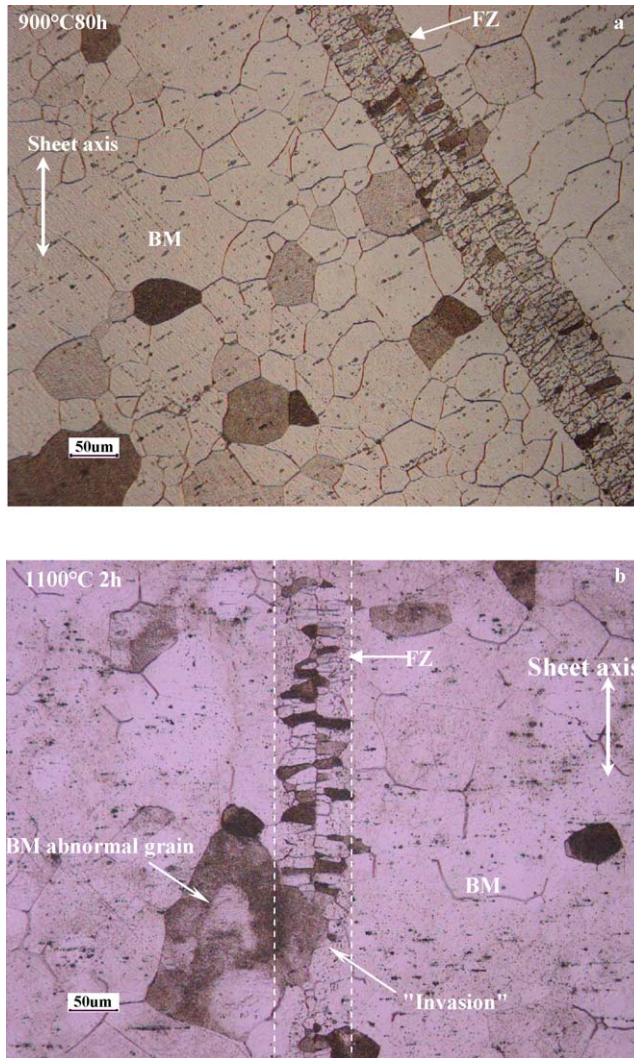


Fig. 6. Optical micrographs of etched bead-on-plate containing sample microstructure heat treated at 900 °C during (a) 80 h and 1100 °C during (b) 2 h, the sections are almost parallel to the main sheet axis; observe an enhanced grain growth in the base metal (BM) vs. grain size reduction in the fusion zone (FZ) by primary recrystallization, at 1000 °C, however, some of the abnormal BM grains invade the FZ grains.

growth in the BM is so pronounced that the grains seem to invade the FZ. Actually, only abnormal grains can progress inside the FZ since their boundaries are bent in such away that the center of curvature is directed toward the fusion zone. In this way, the fusion zone grains become equiaxed and shrink until vanishing at the center line.

The second mechanism correlated to the effect of precipitates is elucidated in the microstructures reported in Fig. 7a and b. Even after ageing at high temperature and long periods of time, the BM and FZ still show a noticeable difference in terms of AlN density and topology. In the BM, the carbides are preferentially intergranular and may be formed during cooling; hence, they have no noticeable effect on the grain growth. The AlN particles increase in size by coalescence and continue to be aligned in the rolling direction. In the FZ, the AlN precipitation is denser and more homogeneous, thus increasing the mobility off the grain boundaries.

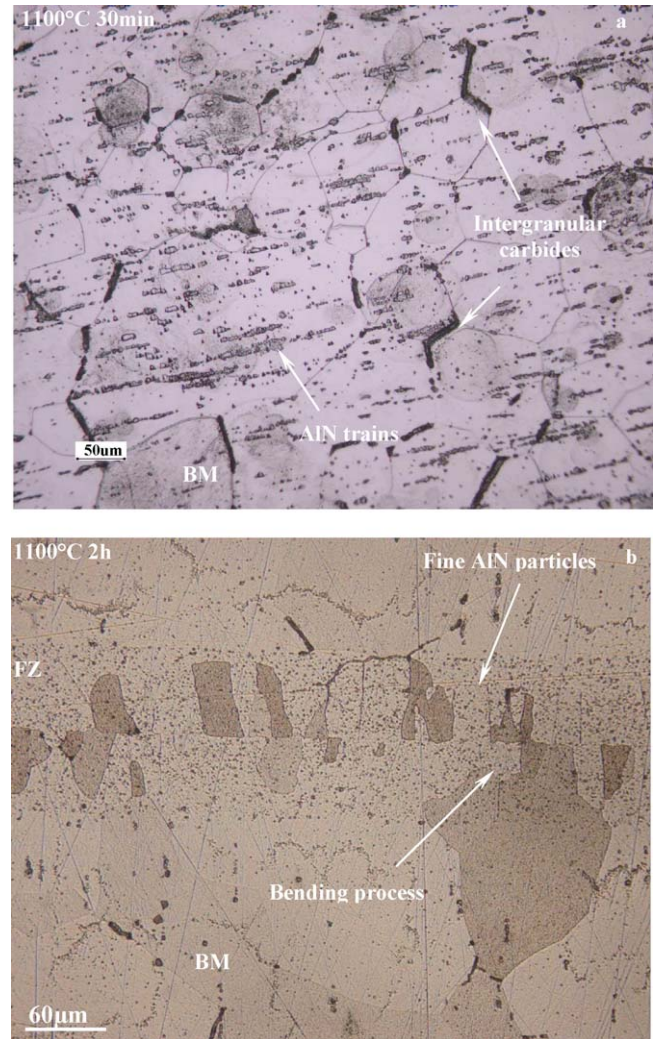


Fig. 7. Optical micrographs of: (a) etched base material microstructure after heating during 30 min at 1100 °C and (b) of etched bead-on-plate containing sample after heating at 1100 °C during 2 h. The sections are almost parallel to the main sheet axis; observe that the base metal (BM) keeps the same precipitation topology of AlN while in the fusion zone (FZ) the fine AlN precipitates scarcely coalesce.

## 4. Mechanical behavior

### 4.1. Experimental

The tensile and creep behaviors of the Fe–Cr–Al alloy after laser melting are studied using welds obtained in the optimized-irradiation conditions. Since extracting micro-tensile coupons is not feasible, we resort to the use of cross-welded samples (CWS) comprising large fractions of bead-on-plate welds produced on 95 µm thick sheets. The volumetric fraction chosen in this study is 0.3, which is high enough to easily differentiate between the mechanical responses of the BM and laser seams and small enough to minimize the residual stresses and eliminate the interaction between the seams. Seams parallel to the mechanical specimen axis (designed as WPA samples) are achieved in order to maintain a theoretically equal strain level between the base material and the weld lines, whereas seams perpendicular to

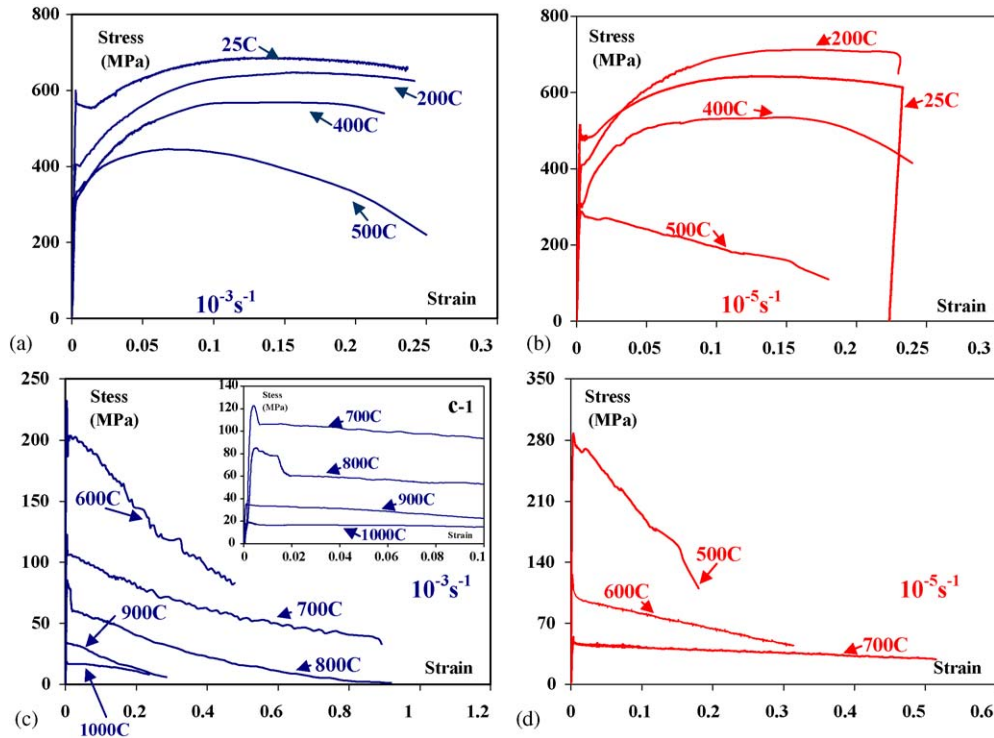


Fig. 8. Stress–strain curves for the BM at two different strain rates: (a and c)  $10^{-3} \text{ s}^{-1}$ , (b and d)  $10^{-5} \text{ s}^{-1}$ , and two temperature ranges: (a and b) between 25 and 500 °C and (c and d) between 500 and 1000 °C.

the sample axis (designed as WPE samples) permit the stresses in the base material and the weld to start identical. All the tests are conducted in air and the samples are heated in a three-zone radiation furnace. Prior to the mechanical testing, all samples were slightly polished on both sides by a 1200-grit SiC paper in order to flatten the weld humps.

## 4.2. Results and discussions

### 4.2.1. Base material under tensile

Fig. 8a–d show the engineering stress–strain curves for the BM obtained in tension at temperatures ranging from 25 to 1000 °C and at two strain rates of  $10^{-3}$  and  $10^{-5} \text{ s}^{-1}$ . At room temperature, a pronounced static strain ageing (SSA) is systematically produced for both strain rates. However, the yield stress is more important for  $10^{-3} \text{ s}^{-1}$  than for  $10^{-5} \text{ s}^{-1}$  (Fig. 9a), which implies a time-dependent characteristic of the SSA phenomenon, leading to an increase in the ultimate strength for increasing strain rate. The SSA extent decreases with increasing the temperature [13], and concomitantly, the strain hardening rate increases, but independently of the strain rate. This phenomenon and the “apparent” viscoplastic behavior of the SSA effect, both, induce an abnormal intersection between the stress–strain curves obtained at 25 and 200 °C for a strain rate equal to  $10^{-5} \text{ s}^{-1}$ , leading to a more important tensile resistance at 200 °C than at 25 °C (Fig. 8b). Observe a maximum hardening rate when the SSA vanishes (at approximately 500 °C for  $10^{-3} \text{ s}^{-1}$  and at 400 °C for  $10^{-5} \text{ s}^{-1}$ ) (Fig. 8a and b).

The SSA occurs when interstitial or substitutional elements segregate at dislocations and immobilize them [14,15]. The yield

point effect reflects the difficulty for the dislocations to escape from these obstacles. Actually, the mechanism proceeds in a repeated breakaway of dislocations from Peierls potential hills and their recapture by mobile solute clouds until enough strain localization multisites are produced to induce a sudden load drop by propagation of Lüders bands. On one hand, this mechanism is thermally activated, so the yield point extent decreases with increasing the temperature. On the other hand, higher strain rates induce a more homogeneous repartition of stresses in the sample [16], lessening shear localization sites. As such, the onset of Lüders band propagation is retarded, and the yield stress increases.

In the range of high temperatures, the SSA effect reappeared in the stress–strain curves, but a secondary continuous drop of the load immediately follows the primary drop associated with the propagation of Lüders bands (Fig. 8c and d). Therefore, the continuous decrease in the load is attributed to the sample necking that was initiated by the sudden multiplication of Lüders bands. In fact, at these temperatures, the recovery predominates at the expense of hardening, thus facilitating strain localization.

The extent of the yield point effect increases with the temperature, reaching a maximum value at 800 °C (Fig. 8c-1). The ductility of the material shows similar trend, i.e. reaches a maximum value (100%) at approximately 800 °C before a significant decrease at 900 and 1000 °C (Fig. 9b). Both behaviors can be explained by intergranular chromium carbide and titanium carbonitride precipitations (Fig. 10) and grain growth phenomena that take place at temperatures above 820 °C. In fact, on one hand, this precipitation reduces the concentration of free elements, rendering the dislocations more mobile in the matrix,

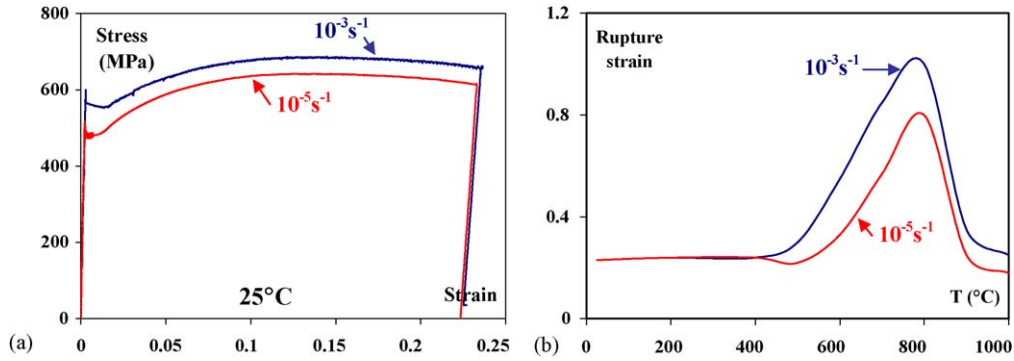


Fig. 9. (a) Stress–strain curves of the BM at two different strain rates revealing the apparent viscoplastic behavior at room temperature and (b) ductility of the BM at two strain rates for temperatures ranging from 25 to 1000 °C.

and as such, diminishing the magnitude of SSA. On the other hand, intergranular precipitates can significantly lower the ductility of the material by hindering grain sliding and promoting the nucleation of intergranular damage-induced pores. In foils, grain growth rapidly leads to columnar microstructures, and as such, a misoriented grain with respect to the applied stress can alone generate a fully penetrated defect causing the immediate failure of the sample.

#### 4.2.2. Comparison between the BM, WPE and WPA behaviors under tensile

Figs. 11a, 11c, 12a, and 12c compare the stress–strain curves of the BM and WPE at various temperatures and strain rates, while Figs. 11b, 11d, 12b, 12d, 13b, 13d, and 14 compare the stress–strain curves of the WPE and WPA at the same ranges of temperatures and strain rates. With increasing the temperature, three main consistent trend disparities occur between these three materials:

- (1) The WPA and WPE show higher tensile strength than the BM, and this effect becomes more pronounced with increasing temperature;
- (2) In the range of low temperatures, no SSA effect is produced for the WPE and WPA (Figs. 11 and 12). The WPE has a slightly lower yield stress than the WPA, but both materials nearly present the same strain hardening rate except for the case of 500 °C at  $10^{-5} \text{ s}^{-1}$  (Fig. 12);
- (3) In the high temperature range (500 °C for  $10^{-5} \text{ s}^{-1}$  and 600 °C for  $10^{-3} \text{ s}^{-1}$ ), the BM and the WPA show a systematic softening after the yield point, while the WPE shows hardening for all temperatures and strain rates (Figs. 13 and 14). The WPE ductility is considerably lower than that of the BM and WPA for all temperatures and strain rates.

These effects can be respectively explained as follow:

- (1) The globular morphology and the size of the AlN precipitates homogeneously dispersed in the FZ suggest that they form coherent interfaces with the surrounding matrix. As such, the FZ shows more structural hardening than the BM. We may therefore suggest an Orowan mechanism to bypass

the particles as in the Fe–Cr–Al ODS-based alloys [16]. This strengthening effect, being a thermally activated mechanism, becomes more marked with increasing the temperature. To illustrate this strengthening effect, the constitutive behavior of the FZ was extracted based on the experimental data obtained for the BM and the WPE (Fig. 15).

The methodology involves development of numerical solutions to inverse problems using a Levenberg-type optimization. In fact, to solve the inverse problem of the constitutive behavior computation, a stress–strain curve for the FZ is first assumed. Knowing the geometry and constitutive behavior of the BM (which was also calculated by an inverse method), a stress strain curve for the WPE is generated using elastic–plastic 2D finite element analysis. This computed stress–strain curve is compared with a WPE experimental curve, and the initial elastic–plastic 3D parameters are modified and updated following the Levenberg objective function. This process is repeated until a satisfactory agreement is reached between the computed curve and the experimental WPE stress–strain curve.

In these calculations, the total deformation was taken as the sum of elastic and plastic strain tensors:

$$\tilde{\varepsilon} = \tilde{\varepsilon}^e + \tilde{\varepsilon}^p, \quad \tilde{\sigma} = \tilde{C} : \tilde{\varepsilon}^e \quad (1)$$

where  $\tilde{C}$  is the fourth rank of the elastic tensor. The criterion is given by Eq. (2) where  $J_2$  is the second invariant of the stress tensor:

$$f(\tilde{\sigma}) = J_2(\tilde{\sigma}) - R \quad (2)$$

The normality rule provides the plastic flow rule:

$$\tilde{\varepsilon}^p = \dot{p} \frac{\partial f}{\partial \tilde{\sigma}}, \quad \dot{p} = \dot{\varepsilon}_0 \exp\left(-\frac{E_a}{k_B T}\right) \exp[\langle f(\tilde{\sigma}) \rangle V_a / (k_B T)] \quad (3)$$

where  $\dot{p}$  is the viscoplastic multiplier and  $\langle f(\tilde{\sigma}) \rangle$  means the maximum of  $(f(\tilde{\sigma}), 0)$ . The latter equation is used to simulate the apparent viscoplasticity of the material, where  $T$  is the absolute temperature,  $V_a$  the activation volume, and  $E_a$  is the activation energy [17]. The strain hardening is assumed to be isotropic without kinematic hardening fol-

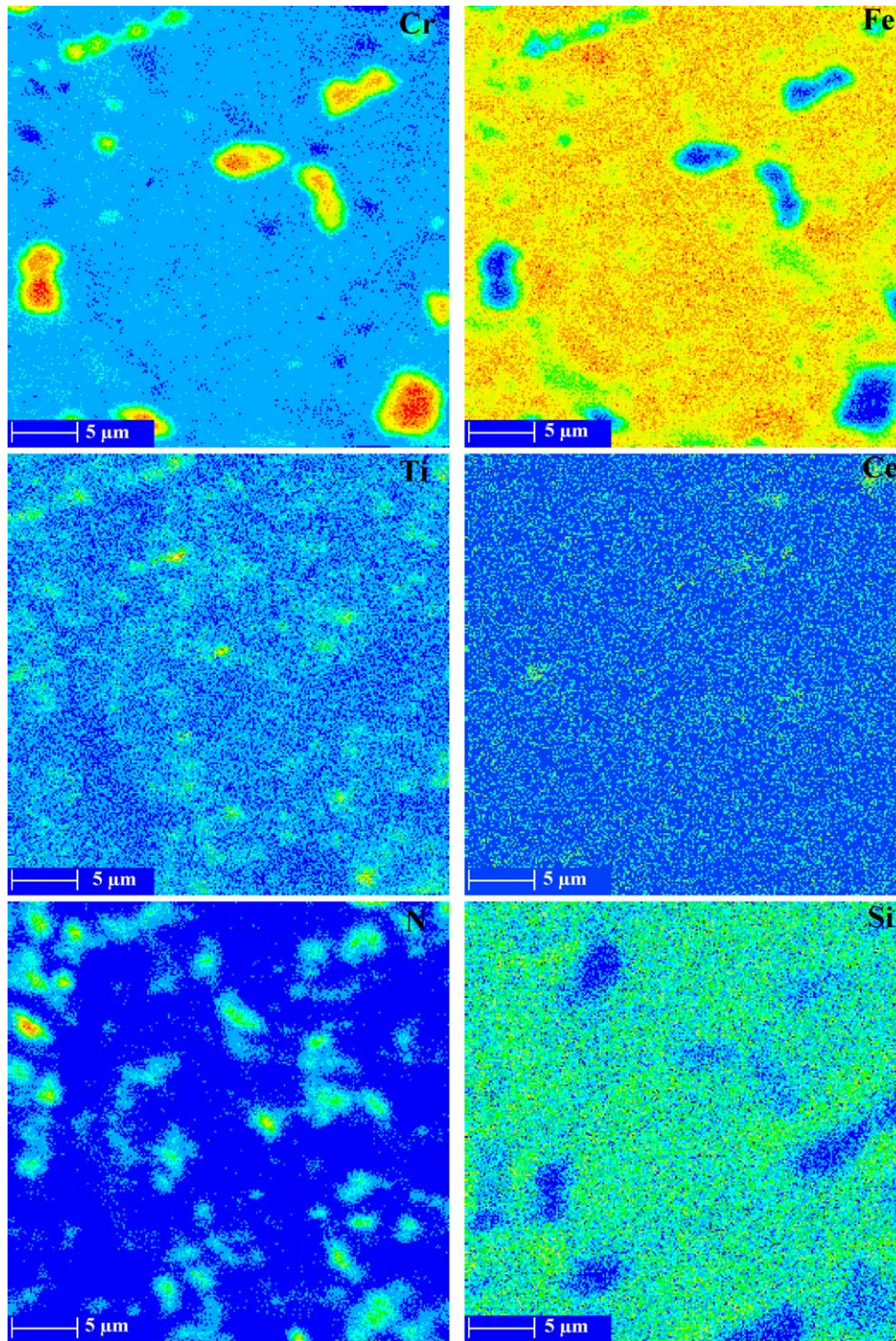


Fig. 10. EPMA X-ray maps of a same region from a BM cross-section revealing enhanced intergranular precipitation of chromium- and titanium-rich carbonitrides.

lowing a non-linear double law:

$$R = R_0 + Q_1(1 - \exp(-b_1 p)) + Q_2(1 - \exp(-b_2 p)) \quad (4)$$

A constitutive Norton creep-type law is also introduced for temperatures higher than 300 °C.

The results of simulations, illustrated in Fig. 15, demonstrate that laser welding generates a microstructure with significant improvement in the tensile resistance.

- (2) The WPE and WPA show a continuous tangent modulus-type curves, which are generally attributed to a plastic strain progressively and partially affecting the grains. At the start, the dislocations are mobile in grains favorably orientated with respect to the applied stress. The strain increases until all the grains in the sample gage length incur plasticity. Hence, the fact that no stress jump is produced in the WPE and WPA curves for a volume fraction of FZ equal to 0.3, suggests that an interaction occurs between the laser seams and the BM behaviors. Actually, Muller et al. [18] reported

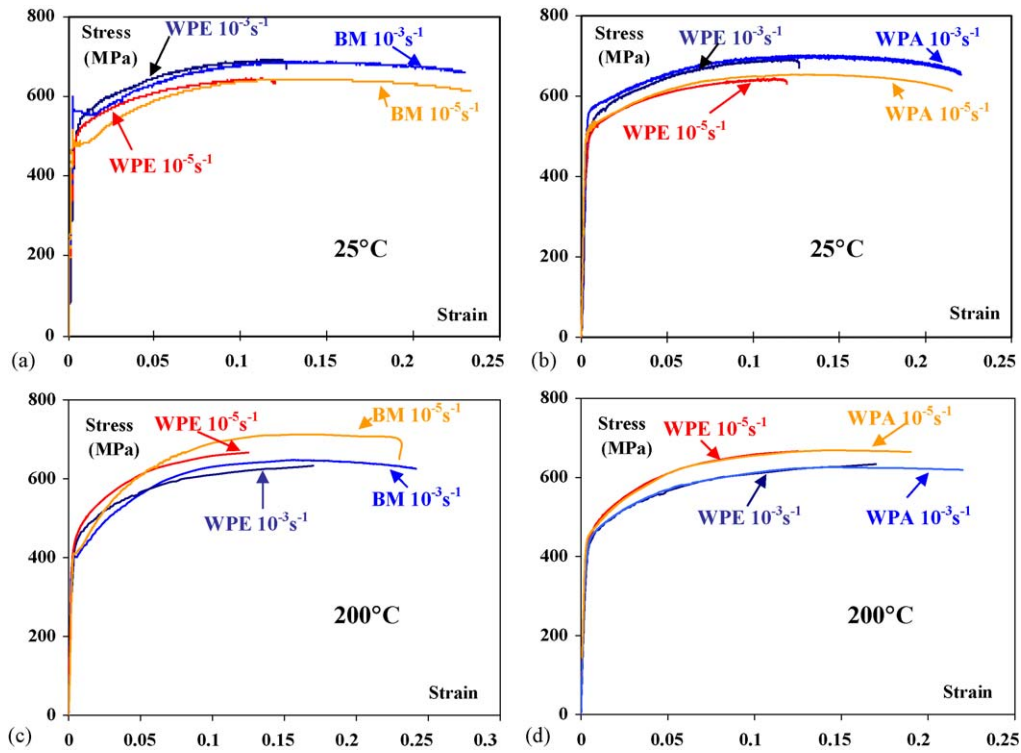


Fig. 11. In (a) and (c) are shown stress–strain curves for the BM and the WPE recorded at  $10^{-3}$  and  $10^{-5} \text{ s}^{-1}$  strain values for 25 and 200 °C, respectively; in (b) and (d) are shown stress–strain curves for the WPE and WPA at two different strain rates for 25 and 200 °C, respectively.

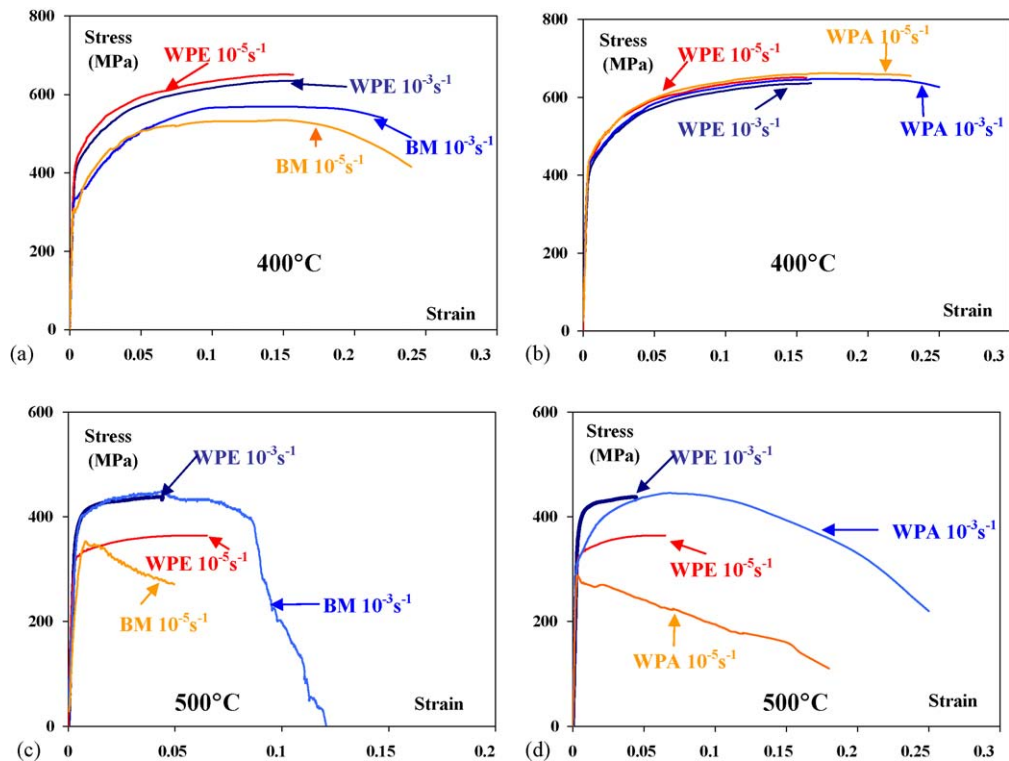


Fig. 12. In (a) and (c) are shown stress–strain curves for the BM and the WPE recorded at  $10^{-3}$  and  $10^{-5} \text{ s}^{-1}$  strain values for 400 and 500 °C, respectively; in (b) and (d) are shown stress–strain curves for the WPE and WPA at two different strain rates for 400 and 500 °C, respectively.

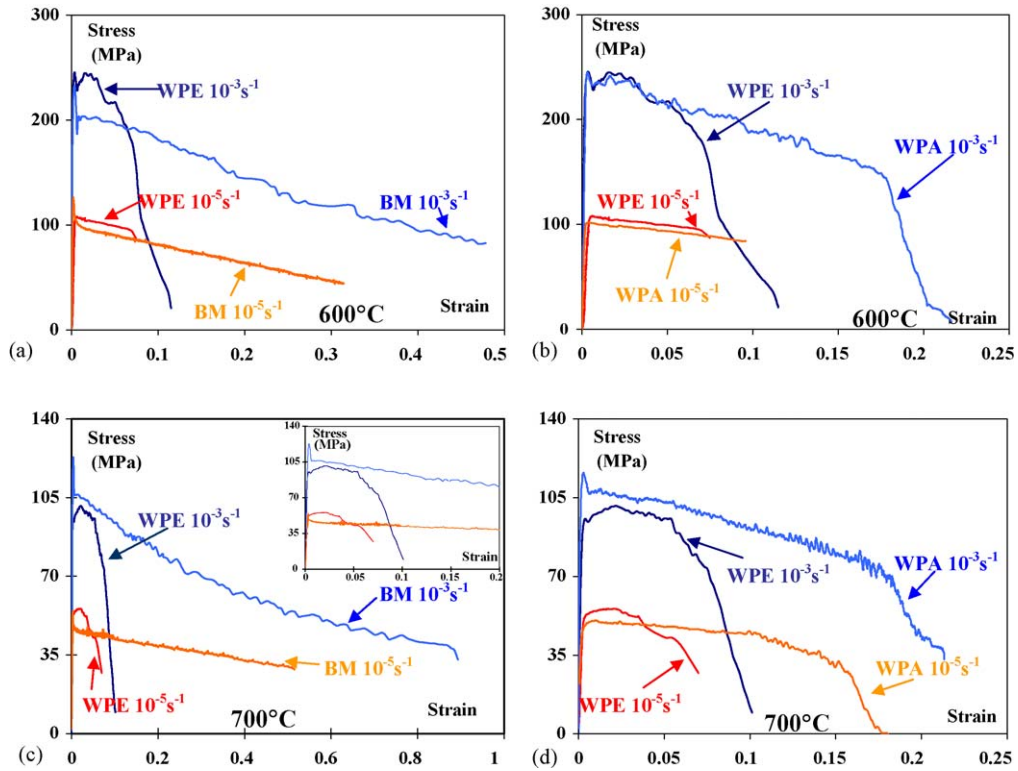


Fig. 13. In (a) and (c) are shown stress–strain curves for the BM and the WPE recorded at  $10^{-3}$  and  $10^{-5}$   $s^{-1}$  strain values for 600 and 700 °C, respectively; in (b) and (d) are shown stress–strain curves for the WPE and WPA at two different strain rates for 600 and 700 °C, respectively.

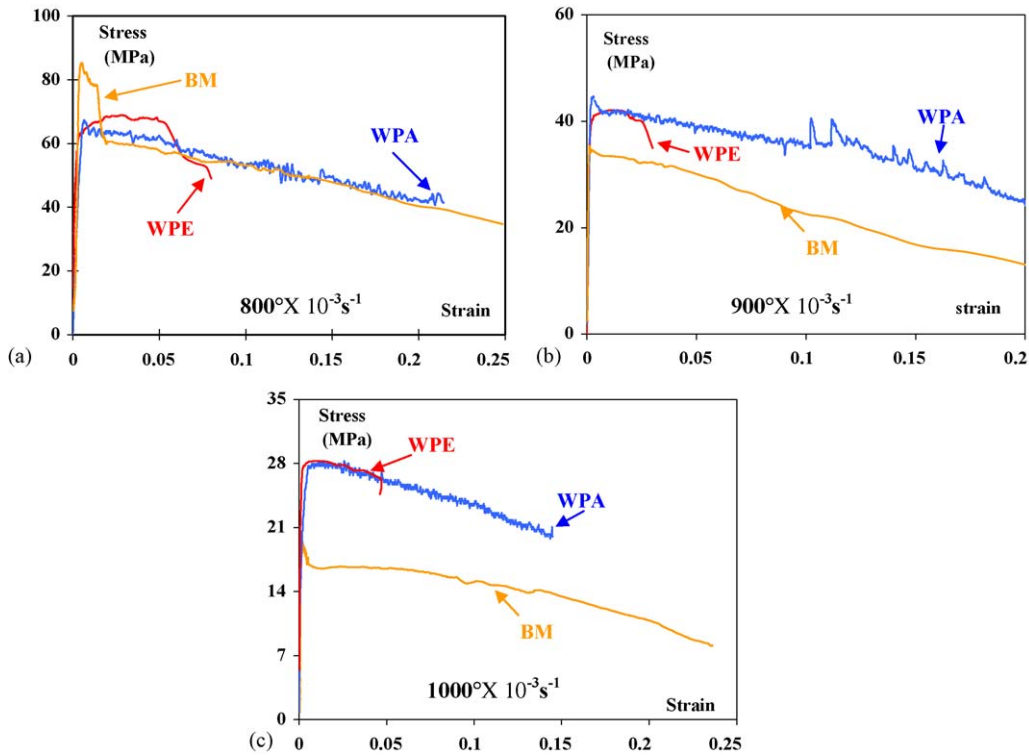


Fig. 14. Stress–strain curves for the BM, WPE and WPE samples at  $10^{-3}$   $s^{-1}$  strain rate and for: (a) 800 °C, (b) 900 °C, and (c) 1000 °C.

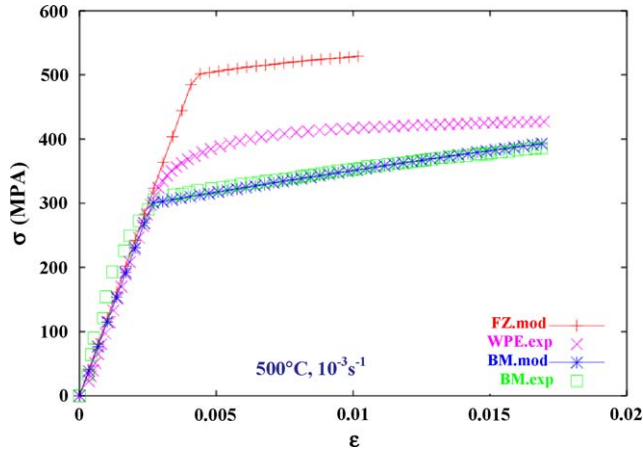


Fig. 15. Inverse method-type optimization results showing the stress–strain curve of the FZ in the WPE sample tested at 500 °C and  $10^{-3} \text{ s}^{-1}$  strain rate up to 0.012 asymptotic cumulated strain in the BM.

for continuous-wave laser welds that while the BM encloses compressive residual stresses, the HAZ and FZ are subjected to tensile residual stresses that have higher magnitude. As such, under tensile loading, the plastic strain and dislocation mobility arises at a lower stress level in the WPE and WPA; hence, the SSA is reduced. The onset of plasticity occurs,

however, earlier in the WPA than in the WPE. This is probably due to the mismatch between the BM and the FZ/HAZ, as the FZ is harder than BM. The mismatch creates stress concentration at the FZ/HAZ/BM interfaces in the WPE, but not in the WPA samples (Fig. 16), and as such, the yield stress is lower for the WPE than for the WPA. The strain hardening rate is, nevertheless, roughly the same in the WPE and WPA, indicating that the grain texture and morphology have no influence on plasticity mechanisms under tensile loading. An intriguing effect occurs in the WPE and WPA samples for  $T \geq 500 \text{ }^\circ\text{C}$ . At these temperatures, the BM shows minimal strain hardening for  $10^{-5} \text{ s}^{-1}$  due localized necking, which leads to discuss the third point.

(3) In fact, while the WPA exhibits the same softening phenomenon as the BM, independently of the strain rate (but with higher yield stress), the WPE displays strain hardening for all temperatures and strain rates, before a crack suddenly initiates at the sample edge lowering the ductility. Fig. 16b depicts Von Mises stress contour in the WPE configuration loaded in tension up to a 0.006 asymptotic cumulated strain at 500 °C and  $10^{-5} \text{ s}^{-1}$  strain rate. In this finite element simulation, the constitutive behavior used for the FZ was that extracted by the inverse method described earlier. The stress distribution along an edge of the sample near the MB/FZ interface is plotted in the graph of Fig. 16a.

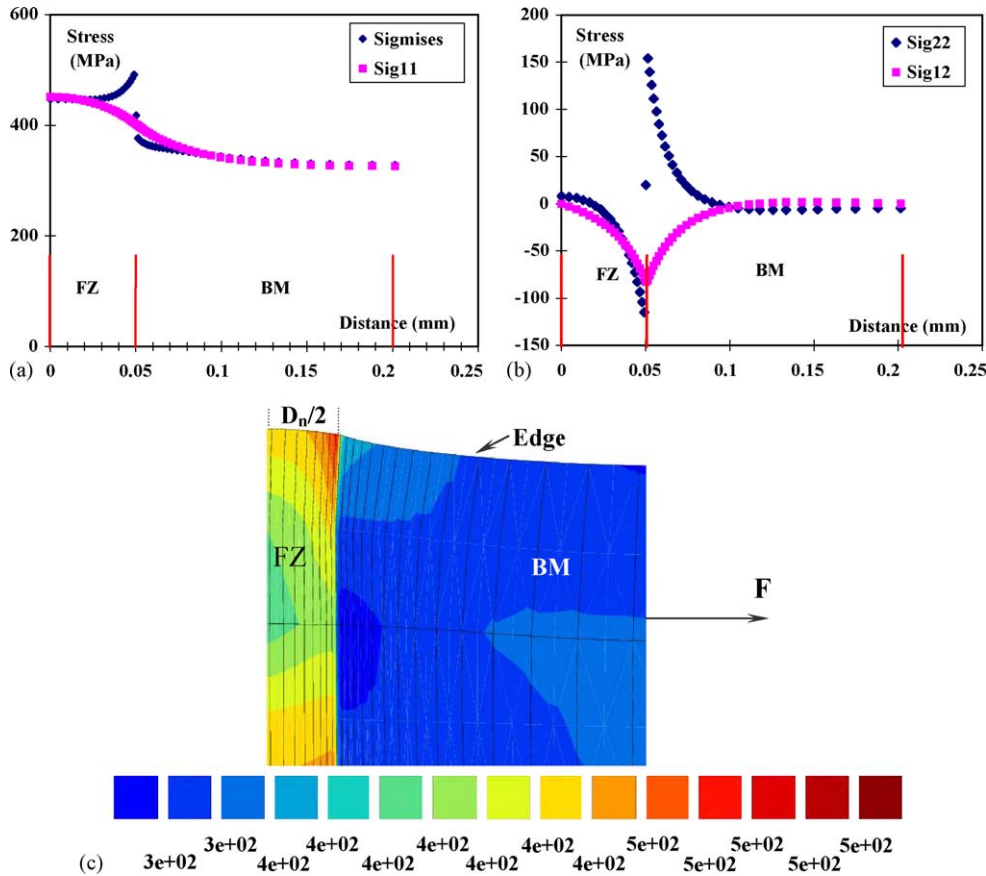


Fig. 16. Finite element calculations using ZeBuLon: (a) Von Mises stress and uniaxial stress distributions, for 0.006 asymptotic total strain at the BM, along the gage length edge of a WPE sample loaded at 500 °C and  $10^{-3} \text{ s}^{-1}$  strain rate, (b) shear and normal stress distributions along a gage length edge of a WPE sample tested at the same loading conditions of Fig. 27a, and (c) Von Mises stress contour in a WPE sample tested under the same loading conditions of Fig. 16a.

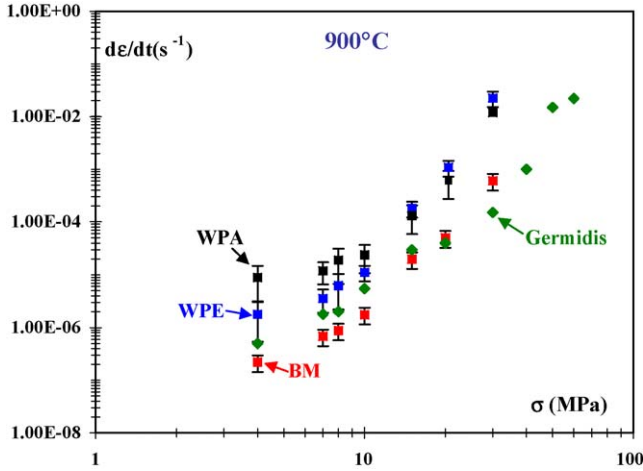


Fig. 17. Creep stress–strain rate plots of the BM, WPA and WPE at 900 °C in comparison with those reported by Germidis [1] for an ultra low carbon containing Fe–Cr–Al sheet with 235 μm in thickness. The strain rates are calculated at the beginning of the steady-stage regime with less than 10% variation.

Along the edge of the gage length, the uniaxial component  $\sigma_{11}$  is equal at 450 MPa at the FZ center, is 400 MPa near the interface, and reaches 320 MPa at the BM. The material mismatch is maximal for the  $\sigma_{22}$  component, which changes from a compressive state in the FZ (–150 MPa) to a tensile state in the BM (150 MPa). This strong triaxiality, which can induce a premature crack opening at the edge of the sample, accounts for the ductility drop that only affects the WPE sample. Thus, no stabilized necking can occur for the WPE as the seams laid perpendicularly to the loading axis impede the contraction of the sample.

#### 4.2.3. Comparison between the BM, WPE and WPA behaviors under tension-creep

The results of creep tests are interpreted and reported in form of stress–strain rate plots shown in Fig. 17. The strain rates are measured at the beginning of the steady-stage in order to avoid integrating the mechanical contribution of the thermally grown oxide layer, which may also induce significant scatter. This beginning is set for a relative strain variation that does not exceed 10% during 1 h creep. The creep tests are performed on the BM, WPE and WPA samples at 900 °C for seven stress values: 4, 7, 8, 10, 15, 20 and 30 MPa, covering two stress domains reported both by Dionnet [19] and Germidis [1]:

- (1) *Low stress domain* (< 10 MPa), where the strain rate variation is most likely controlled by an interfacial reaction mechanism. Several governing equations are suggested to account for this mechanism, but the most frequent law is that reported by Artz and Ashby [20,21]:

$$\dot{\epsilon}^{\text{irc}} = \frac{14D_{\text{eff}}\Omega(\sigma - \sigma_{\text{tr}}(T))}{kTd^2 \left(1 + \frac{12b\mu}{d(\sigma - \sigma_{\text{tr}}(T))} \frac{D_{\text{eff}}}{\alpha D_b}\right)} \quad (5)$$

where  $d$  is the grain size,  $\mu$  the shear modulus,  $D_{\text{eff}}$  the effective diffusion coefficient linked to the lattice diffusion coefficient, which allows for the diffusion along the disloca-

tion core,  $\sigma_{\text{tr}}$  is the stress threshold, and  $\alpha$  is a key parameter quantifying the partition between the diffusional flow creep and interfacial reaction control creep. For Fe–Cr–Al alloys, this law was used because the carbon tends to preferentially segregate near the grain boundaries for temperatures below 1000 °C. Hence, the dislocations undergo a viscous drag at/near the grain boundaries, which no longer act as a perfect source and/or sink of vacancies, as traditionally considered in diffusional flow theories. Nevertheless, for simplicity, we have used a classical Norton-type creep law.

- (2) *High stress domain* (>10 MPa). Here the dislocation flow controlled creep is dominant because of the higher loading energy and the lower diffusional relaxation time:

$$\dot{\epsilon}(\sigma) = AD_{\text{eff}} \frac{\mu b}{kT} \left(\frac{\sigma}{\mu}\right)^n \quad (6)$$

$A$  is Dorn's constant and  $D_{\text{eff}}$  is the effective diffusion coefficient:

$$D_{\text{eff}} = D_v \left[1 + \frac{\pi\delta D_b}{dD_v}\right] \quad \text{with}$$

$$D_v = D_{v0} \exp\left(\frac{-Q_v}{RT}\right) \quad \text{and} \quad D_b = D_{b0} \exp\left(\frac{-Q_b}{RT}\right) \quad (7)$$

$\delta$  is the grain boundary thickness and  $D_b$  is the diffusion coefficient at the grain boundary. In determining the model constants we do the following:

- For the low stress range, and in order to relatively account for the diffusional creep mechanisms, we choose to calculate the exponent coefficient  $n$  and lattice activation energy  $Q_v$  for  $A = 1$ ;
- For the elevated stress range, we compute the exponent  $n$  and Dorn's coefficient  $A$ , but using the lattice activation energy  $Q_v$  related to the low stress range.

The other parameters are constants:  $D_{v0} = 2 \times 10^{-4} \text{ m}^2 \text{ s}^{-1}$  (same value as that for  $\alpha$ -Fe);  $\delta D_{b0} = 10^{-12} \text{ m}^3 \text{ s}^{-1}$  ( $\alpha$ -Fe);  $Q_b = 174 \text{ KJ/mol}$ ;  $d = 5 \times 10^{-6} \text{ m}$  (typical value for Fe–Cr–Al-RE);  $\mu$  (900 °C) = 40 GPa (experimental value extracted from the above tensile stress–strain curves);  $b = 2.48 \times 10^{-10} \text{ m}$  ( $\alpha$ -Fe).

The constants are summarized in Table 2.

4.2.3.1. *Discussion on the measured strain rate values.* The steady state strain rate values are in good agreement with those obtained by Germidis [1] using a Fe–Cr–Al foil with a very low interstitial content (60 ppm in weight). The slight shifting, how-

Table 2

Numerical identification of the physics-based creep parameters: activation energy  $Q$ , pre-exponent coefficient  $n$  and Dorn coefficient  $A$

	$\sigma \leq 10 \text{ MPa}$	$\sigma \geq 10 \text{ MPa}$
MB	$n = 2.20, Q_v = 200 \text{ KJ/mol}$	$n = 5.17, A = 5.2 \times 10^{10}$
WP	$n = 1.9, Q_v = 210 \text{ KJ/mol}$	$n = 6.8, A = 5.2 \times 10^{17}$
WP	$n = 1.06, Q_v = 265 \text{ KJ/mol}$	$n = 6.6, A = 5.2 \times 10^{19}$

ever, toward higher values for Germidis' strain rates obtained in the low stress range can be explained by the higher carbon concentration in our material, which generates a higher extent of dislocation drags. The WPE and WPA display a lower creep resistance than that of the BM for all the stresses. These two materials creep nearly at the same rate over the elevated stress range, but for the low strain range the WPA creeps faster.

#### 4.2.3.2. Discussion on the simulated physics-based parameters.

For low stresses, the apparent sensitivity of the stress decreases since the diffusional flow is the dominant creep mechanism. The Norton exponent  $n$  calculated for the BM is nearly 2.5, and naturally follows the fact that we used dislocation-type creep law in a stress range where the atomic diffusion rather dominates the creep deformation. For the WPA, this coefficient is approximately one. This very low value is most likely due the fact that the FZ grains are elongated orthogonally to the loading axis. The diffusional phenomena are accelerated and the cavity-growth induced damage is more important in the WPA FZ than in the BM and the WPE FZ.

For the elevated stress range,  $n$  dramatically increases, and reaches approximately six for all materials as the steady strain rate increases. The disparities in creep resistance between the three materials are mainly reflected by important deviations in the Dorn constant ( $A$ ) values. Actually, for the BM, we obtain a value slightly higher than that calculated by Germidis, who used an activation energy (240 KJ/mol) related to pure iron, which is greater than that computed in the present study (200 KJ/mol), but associated, however, with a higher exponent value  $n = 7$ .

We outline three possible phenomena that can account for the dissimilarities in the Dorn coefficient between the BM, WPE and WPA:

- (1) The BM undergoes an important amount of secondary recrystallization. The continuous increase in grain size will generate a consistent improvement in creep resistance. This effect increases with decreasing stress since the longer primary-creep stage generates more important secondary recrystallization;
- (2) While the BM is increasingly strengthened, the FZ grain boundaries seem to be completely pinned and even multiplied by a possible residual stress induced primary recrystallization mechanism. So, the FZ will tend to creep increasingly faster due to more stable and denser grain boundaries;
- (3) The dynamic recrystallization can also contribute to intensify the strengthening process of the BM. Actually, Carel et al. [22] show that the strain energy accelerates grain growth by some micromechanisms driving the selection of favorable crystallographic orientations;
- (4) Oqab and Monceau [23] show by in situ observations under an environmental SEM that most of the oxidation induced cavities nucleate during the heating process up to the soaking period. Hence, damage obviously contributes in the strain rate values calculated at the onset of steady-stage creep. This contribution will be less important in BM than in the FZ due to the fast grain growth of the BM, which reduces the nucleation as well as the growth of interfacial

cavities. Creep testing should then be preferably performed under high vacuum environment to limit the cationic oxidation process;

- (5) The faster grain growth in the BM than in the FZ will induce less chromium carbide precipitation, and hence free more carbon extent in the BM. In particular, the dislocation drag process will be more marked in the BM than in the FZ, amplifying the creep resistance gap.

## 5. Conclusions

Uniaxial tension and creep properties of as received and laser micro-welded thin Fe–Cr–Al foil were studied and interpreted over a wide range of temperatures through various methods of characterization and evaluation. These methods include optical microscopy, scanning electron microscopy, transmission electron microscopy, heat treatment in a vacuum, electron probe microanalyses and finite element simulations of the laser welding process and deformation. The laser bead shows higher tensile resistance than the base material, because of a dense repartition of fine and coherent aluminum nitrides (AlN) in a fine basaltic microstructure generated due to uncharacteristic high cooling rates. The precipitates may strengthen the material by inducing attractive junction networks similar to those engendered in Fe–Cr–Al ODS alloys. The static strain ageing effect observed in the base material is eliminated for the laser bead due to the combined effects of residual stresses and reduction of mobile interstitial free solute elements by enhanced AlN and Cr<sub>23</sub>C<sub>6</sub> precipitates. At higher temperatures, the bead creeps significantly faster than the base material, because of grain refinement in the weld, driven by primary recrystallization and recovery, against important grain growth in the base material driven by secondary recrystallization. This mismatch is more pronounced when the weld center line is aligned with the applied stress, but only for stresses below 10 MPa, because of a more important cavity-growth driven by diffusional creep. This study provides a new and more complete database for the mechanical behavior of thin ferritic foil microstructures. Furthermore, it validates a novel technology for real-time assembling of honeycomb structures with significant increase in productivity required for the growing market of catalytic converters.

## Acknowledgments

Jean Favennec and Marc Dubus from ArvinMeritorRosi are to be thanked for their financial support and material supply. Center des Materiaux at Ecole Nationale Supérieure des Mines de Paris also supported this work.

## References

- [1] A. Germidis, Doctoral Thesis, Centre des Matériaux, Ecole Nationale Supérieure des Mines de Paris, ENSMP, 1996.
- [2] W. Maus, Proceedings of the MACC Conference, Wuppertal, Germany, October 27–28, 1997, pp. 3–16.
- [3] Emission Control Components and Materials, US industry study with forecasts to 2007 & 2012, 2003. Website: <http://www.freedoniagroup.com/pdf/1678web.pdf>.

- [4] H. El Kadiri, R. Molins, Y. Bienvenu, *Mater. Sci. Forum* 461–464 (2004) 1107–1116.
- [5] J.D. Bartout, Y. Bienvenu, J. Favennec, M. Dubus, *Bulletin du Cercle d'études des métaux*, tome XVI, no. 14, p. 191, 1997.
- [6] S. Okabe, M. Khono, K. Ishii, M. Yukumoto, T. Nozaki, *Mater. Sci. Eng. A* 181–A182 (1994) 1104–1108.
- [7] Discussion with Marc Dubus at ArvinMeritorRosi, Dreux, France.
- [8] H. El Kadiri, M. Dahmen, Y. Bienvenu, T. Malot, M.F. Horstemeyer, *Proceedings of the 23rd International Congress on Applications of Lasers & Electro-Optics*, October 2004.
- [9] H. El Kadiri, R. Molins, Y. Bienvenu, *Mater. Sci. Forum* 461–464 (2004) 1157–1164.
- [10] H. El Kadiri, R. Molins, Y. Bienvenu, M.F. Horstemeyer, *Oxid. Met.* 64 (1–2) (2005) 63.
- [11] H. El Kadiri, R. Molins, M.F. Yves Bienvenu, Horstemeyer, *Oxid. Met.* 64 (1–2) (2005) 99.
- [12] H. El Kadiri, *Doctoral Thesis*, Centre des Matériaux, Ecole Nationale Supérieure des Mines de Paris, ENSMP, 2004.
- [13] A. Van den Beukel, *Phys. Stat. Solid* 30 (1975) 197–206.
- [14] Y. Estrein, L.P. Kubin, *J. Phys. III* 1 (1991) 929–943.
- [15] G. Merceron, *Doctoral Thesis*, Centre des Matériaux, Ecole Nationale Supérieure des Mines de Paris, ENSMP, 2000.
- [16] Y. Estrein, S. Zhang, P.G. McCormick, *Acta Mat.* (2000) 1087–1094.
- [17] K. Muller, J.P. Bergmann, H.W. Bergmann, *Mater. Res. Adv. Tech.* 92 (3) (2001) 253–259.
- [18] B. Dionnet, *Doctoral Thesis*, Université de Limoges France, 1993.
- [19] M.F. Artz, M.F. Ashby, R.A. Verral, *Microscopic Aspects of Diffusion Creep*, CUED/C/MATS-TR-60, 1982.
- [20] M.F. Ashby, R.A. Verall, *Acta Mat.* 21 (1973) 149.
- [21] R. Carel, C.V. Thompson, H.J. Frost, *Acta Mat.* 44 (6) (1996) 2479–2494.
- [22] D. Oqab, D. Monceau, *Scripta Mater.* 44 (2001) 2741–2746.